Revisiting competing paths in electrochemical CO_2 reduction on copper via embedded correlated wavefunction theory

Qing Zhao[1] and Emily A. Carter[1,2 *]

[1]Department of Mechanical and Aerospace Engineering, Princeton University, Princeton, NJ, 08544-5263, United States

[2]Office of the Chancellor and Department of Chemical and Biomolecular Engineering, University of California, Los Angeles, Los Angeles, CA, 90095, United States

Abstract

We reevaluate two key steps in the mechanism of CO_2 reduction on copper at a higher level of theory capable of correcting inherent errors in density functional theory (DFT) approximations, namely embedded correlated wavefunction (ECW) theory. Here, we consider the CO reduction step on Cu(111), which is critical to understanding reaction selectivity. We optimize embedding potentials at the periodic plane-wave DFT level using density functional embedding theory (DFET). All possible adsorption sites for each adsorbate then are screened with ECW theory at the catalytically active site to refine the local electronic structure. Unsurprisingly, DFT and ECW theory predict different adsorption site preferences, largely because of DFT's inability to properly situate the CO $2\pi^*$ level. Differing preferred adsorption sites suggest that different reaction pathways could emerge from DFT versus ECW theory. Starting from these preferred ECW theory adsorption sites, we then obtain reaction pathways at the plane-wave DFT level using the climbing-image nudged elastic band method to determine minimum energy paths. Thereafter, we perform ECW calculations at the catalytically active site to correct the energetics at each interpolated structure (image) along the reaction pathways. Via this approach, we confirm that the first step in CO reduction via hydrogen transfer on Cu(111) is to form hydroxymethylidyne (*COH) instead of formyl (*CHO). Although the prediction to preferentially form *COH is consistent with that of DFT, the two theories predict quite different structural and mechanistic behaviors, suggesting that verification is needed for other parts of the mechanism of CO_2 reduction, which is the subject of ongoing work.

I. Introduction

Our civilization still depends heavily on the burning of fossil fuels, which pollute the air and produce greenhouse gases that warm the Earth. The electrochemical carbon dioxide (CO_2) reduction reaction (CO_2RR) using excess renewable (midday solar, nighttime wind) electricity to produce useful chemicals, fuels, and materials could contribute in a circular economy that decreases future greenhouse gas emissions.[1-4] Copper (Cu), among other metals examined experimentally, remains the only metal catalyst for electrochemical CO_2RR to produce hydrocarbons, but it requires a high overpotential of ~ -1 V vs. the reversible hydrogen electrode (RHE) to achieve reasonable rates and faradaic efficiency. Cu yields a mixture of products, including methane, ethylene, hydrogen (H_2) gas, carbon monoxide (CO), and formate, among other minor products.[1,5-12] Low efficiency and poor selectivity towards valuable products limit commercial applications of electrochemical CO_2RR.

To provide insights for rational design of more efficient electrocatalysts that increase product selectivity and simultaneously lower applied potentials for CO_2RR, elucidation of reaction mechanisms for CO_2RR on Cu and the critical steps that lead to various hydrocarbon products is foundational. Experiments have demonstrated that the product distribution of CO_2RR on Cu strongly depends on the applied potential.[7,11,12] Kuhl *et al.* reported[12] that only H_2 gas, CO, and formate form at overpotentials less negative than -0.75 V vs. the RHE and that H_2 production dominates. When the overpotential reaches -0.75 V vs. RHE, ethylene and methane are the first hydrocarbons observed but an overpotential of -1.0 V vs. RHE is required for reasonable Faradaic efficiencies. Other C_1-C_3 minor products begin to emerge at this highly negative overpotential, but H_2 still dominates while CO and formate production declines. The product selectivity towards different hydrocarbons also depends on surface structure of the Cu electrode used. Hori *et al.* observed[13] that Cu(111) favors formation of methane whereas the formation of ethylene dominates on Cu(100). Schouten *et al.* further showed[14,15] that at pH 7 both methane and ethylene start forming at -0.8 V vs. RHE on Cu(111) whereas ethylene forms at a lower potential of -0.4 V vs. RHE on Cu(100); ethylene formation peaks at -0.6 V vs. RHE, after which its formation decreases and eventually stops. At a potential of -0.8 V vs. RHE on Cu(100) at pH 7, ethylene production again was observed and accompanied by methane formation. Experiments also clearly identified that CO reduction yields similar product distributions and overpotential dependence to those of CO_2RR, suggesting that CO reduction is

rate-limiting.[15,16] Based on experimental observations, various key intermediates and rate-limiting steps for CO_2RR on Cu catalysts have been proposed: hydroxymethylidyne (*COH, where * indicates an adsorbed species) by Hori *et al.*[16] versus formyl (*CHO) by Schouten *et al.*[11,14] as the key intermediate in forming methane, and CO dimer as the precursor to ethylene by Schouten *et al.*[11,14] However, direct experimental identification of reaction intermediates has not yet been possible and thus the reaction mechanisms and rate-limiting steps remain unclear.

A variety of theoretical efforts mainly based on density functional theory (DFT) calculations have helped identify probable elementary steps involved in methane and ethylene formation on various Cu surfaces. Peterson *et al*. proposed[17] the first full reaction mechanism for methane production on the stepped Cu(211) surface, based on thermodynamics alone, in which the rate-limiting step was predicted to be CO reduction to form *CHO. However, Nie *et al.* evaluated[18,19] reaction barriers and found that forming *COH is more kinetically favorable than forming *CHO for the first step of CO reduction, at least on Cu(111). In their work, adsorbed *H directly reacts with adsorbed *CO, with the entire reaction mechanism to form methane involving

$$^*CO \rightarrow {}^*COH \rightarrow C^* \rightarrow {}^*CH \rightarrow {}^*CH_2 \rightarrow {}^*CH_3 \rightarrow CH_4 \quad (1)$$

The rate-limiting step of *COH formation on Cu(111) was confirmed[20,21] by Xiao *et al.* with further consideration of a constant electrochemical potential and pH. However, Cheng *et al.* predicted[22] the first step of CO reduction instead to be *CHO formation on Cu(100) using *ab initio* molecular dynamics simulations with five layers of explicit water molecules, with their proposed reaction pathway involving

$$^*CO \rightarrow {}^*CHO \rightarrow {}^*CHOH \rightarrow {}^*CH \rightarrow {}^*CH_2 \rightarrow {}^*CH_3 \rightarrow CH_4 \quad (2)$$

CO reduction to hydrocarbon products on Cu(100),[23-25] Cu(111),[25] and Cu(211)[26,27] was predicted to occur via a *CHO intermediate.

All of these theoretical efforts were conducted using DFT approximations (DFAs). In practice, DFAs are plagued by electron self-interaction error,[28,29] among other problems, giving rise to errors in quantities critical for simulating heterogeneous catalysis.[30-33] The incorrect prediction by the DFAs used thus far to study CO_2RR – namely, generalized-gradient approximation exchange-correlation (XC) functionals, *i.e.*, Perdew-Burke-Ernzerhof (PBE),[34] revised Perdew-Burke-Ernzerhof (rPBE)[35], or Bayesian error estimation functional with van der Waals correlation (BEEF-vdW)[36] – of where CO adsorbs on Cu(111) (predicted to be the hollow

site[37-40] versus the directly measured atop site[41,42]) is especially worrisome, suggesting that proposed CO_2RR mechanisms and energetics could be wrongly predicted by these DFAs. The incorrect site prediction by these DFAs is due to the CO $2\pi^*$ orbital being too low in energy because of self-interaction error.[38,43] By contrast, more than a decade ago, Sharifzadeh *et al.*[44] showed that atop-site adsorption of CO on Cu(111) could be reproduced successfully by embedded correlated wavefunction (ECW) theory, which provides a correction to XC error inherent in DFT in the embedded region. Although progress has been made in correctly predicting the CO adsorption site on some metal surfaces within DFAs, by using hybrid XC functionals including some exact exchange,[45,46] meta-generalized-gradient approximation functionals,[39] or van der Waals functionals,[40,47] all of these functionals are still subject to XC errors and thus may not always provide accurate structures or energetics. Moreover, the use of hybrid functionals for metallic systems is not well-founded, given that Hartree-Fock (HF) theory diverges at the Fermi level in metals.[48]

Motivated by Sharifzadeh *et al.*'s success,[44] we are interested in revisiting the entire mechanism of CO_2RR on Cu(111) with ECW theory, to see whether correction of the self-interaction error alters understanding of any part of the mechanisms thus far proposed using DFAs. ECW theory removes error caused by the XC approximation in DFT by adding a correction to the energy calculated as the difference between using a correlated wavefunction theory and a DFA for the embedded region, where the former incorporates exact exchange and multi-reference correlated wavefunctions, which eliminates the HF divergence problem referenced above. We focus here on the CO reduction step on Cu(111), given the experimental observation[15,16] that it is rate-limiting. We use ECW theory to compare the kinetic stabilities of the two controversial steps for CO reduction: forming *CHO ($^*CO + {}^*H \rightarrow {}^*CHO$) versus *COH ($^*CO + {}^*H + H_2O \rightarrow {}^*COH + H_2O$). We examine *H transfer to *CO on Cu(111) because experiments showed[1,12,14,15] that the hydrogen evolution reaction (HER) competes with CO reduction at working potentials, indicating a significant amount of adsorbed *H on the Cu surface. (An alternative proton-coupled electron transfer (PCET) path under consideration as well will be reported elsewhere.) The explicit water molecule shown in the *COH formation pathway originates from a mechanism proposed by Nie *et al.*[18,19] that involves hydrogen shuttling through H_2O; it will be discussed in detail below.

This article is organized as follows: Section II contains computational details; Section III presents ECW predictions of adsorption sites for each adsorbate and barriers for CO reduction to form *CHO and *COH; Section IV offers conclusions.

II. Computational methods

We used a composite approach including both periodic slab DFT calculations and cluster model ECW calculations to revisit the CO reduction step on Cu(111) (Figure 1). First, the interaction between each cluster and its extended environment is recovered via adding to the cluster Hamiltonian an optimized embedding potential derived using density functional embedding theory (DFET)[49-51] at the periodic plane-wave DFT level. Then, all possible adsorption sites for each adsorbate are screened with ECW theory[52] using the clusters subjected to their derived embedding potentials. Unfortunately, optimizing reaction pathways directly with ECW theory is prohibitively expensive. Therefore, the reaction pathways were determined initially at the plane-wave DFT level starting from the preferred ECW adsorption sites and the energetics at each interpolated structure along the reaction pathways subsequently were corrected with ECW theory using the cluster models and derived embedding potentials. The size of the active space in the ECW calculations are benchmarked carefully for both adsorption site and reaction barrier calculations to reach chemical accuracy. Details for periodic DFT calculations, deriving embedding potentials, and cluster ECW calculations are outlined below.

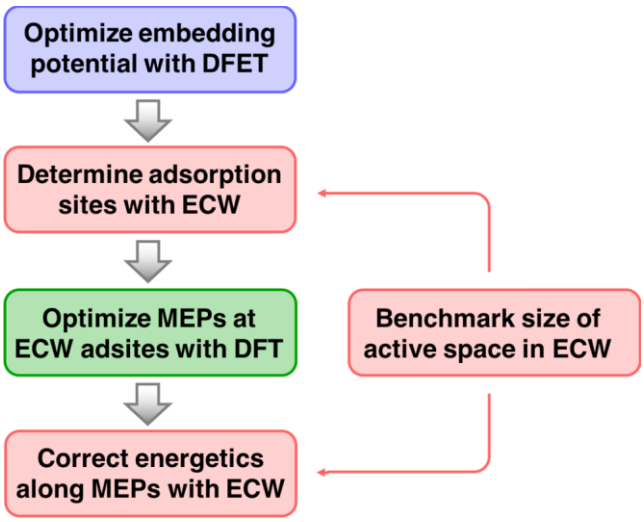

Figure 1. Workflow steps used to study the mechanism for CO_2 reduction on Cu(111): optimizing embedding potentials using DFET (shown in light blue), benchmarking the size of

the active space in ECW theory (light red), determining adsorption sites with ECW theory (light red), optimizing minimum energy paths (MEPs) at ECW-predicted adsorption sites with DFT (light green), and correcting energetics along the MEPs with ECW theory (light red).

Periodic DFT calculations. Periodic Kohn-Sham DFT calculations with the all-electron, frozen-core, projector augmented-wave[53] method and PBE[34] XC functional were performed using the Vienna *Ab initio* Simulation Package (VASP)[54,55] version 5.4.4. Grimme's D3 dispersion correction[56,57] (*i.e.*, DFT-D3) with the Becke-Johnson damping function[58] were included in the DFT calculations. The 1*s* electron of H, the 2*s* and 2*p* electrons of C and O, and the 4*s* and 3*d* electrons of Cu were treated self-consistently. A 3×3 supercell containing a five-layer, 45-atom Cu slab was used to model the Cu(111) surface, with at least 15 Å of vacuum included in the periodic cell. The lattice constant was fixed at the DFT-PBE-D3 optimized bulk value for fcc Cu. The atoms in the three topmost layers were relaxed while the atoms in the two bottommost layers were fixed at their bulk atomic positions. Relaxing atoms in the two topmost layers only, while fixing atoms in the three bottommost layers, reproduced the DFT-PBE-D3 reaction energies for the *CHO and *COH paths to within 0.001 eV. We applied dipole-field energy and potential corrections[59] to cancel the artificial field between the slabs imposed by the periodic boundary conditions. In geometry optimizations, the atoms were relaxed until the maximum residual forces on the atoms were smaller than 0.03 eV/Å. A plane-wave basis set with a kinetic-energy cutoff of 660 eV was used. To sample the Brillouin zone, Γ-point-centered Monkhorst-Pack[60] 14×14×14, 5×5×1, and 3×3×1 *k*-point grids were applied for the bulk unit cell and the 3×3 and 5×5 periodic slab supercells, respectively. These numerical parameters yield total energies converged to within 1 meV/atom, with respect to the kinetic-energy cutoff (660 eV vs. 900 eV) and *k*-point grids (bulk: 14×14×14 vs. 28×28×28; 3×3 slab: 5×5×1 vs. 10×10×1; 5×5 slab: 3×3×1 vs. 6×6×1). Electronic states were occupied using the Methfessel-Paxton method[61] for Brillouin zone integration with a smearing width of 0.09 eV to aid self-consistent field convergence. The minimum energy paths (MEPs) were optimized using the climbing image nudged elastic band (CI-NEB) method[62] with an artificial spring force constant of 3 eV/Å^2 along the reaction tangents. We define the reaction coordinate along the MEP as the cumulative distance between the images on the reaction path,

$$\mathrm{RC}(n) = \sum_{i=0}^{n-1} \left| r_{i+1} - r_i \right| \tag{3}$$

in which RC(n) is the reaction coordinate at the n-th image (n>0 and image 0 is the reactant) and r_i represents the position of all of the atoms at image i. We show the geometries along the reaction path for both *CHO and *COH pathways in the Supporting Information (SI), Figures S1-S2.

DFET embedding potentials. In DFET,[49-51] the total system typically is partitioned into two subsystems, a cluster and its environment. The interaction between the cluster and its environment is recovered by the embedding potential, V_{emb}. We used a Cu_{12} cluster (Figure 2a) to compute V_{emb} for the *CO adsorption site; a Cu_{11} cluster (Figure 2b) to compute V_{emb} for the *H and *CHO adsorption sites, and for the CO reduction reaction to form *CHO; and a Cu_{11} cluster (Figure 2c) to compute V_{emb} for the *COH adsorption site and the CO reduction reaction to form *COH. The clusters are carved out of a 5×5 four-layer 100-atom Cu slab (Figure 2d). We determined the embedding potential, V_{emb}, at the periodic DFT level using a modified VASP version 5.3.3 by maximizing the extended Wu-Yang functional[63] with respect to V_{emb},

$$W\left[V_{emb}\right] = E_{cluster}\left[r_{cluster}\right] + E_{env}\left[r_{env}\right] - \int V_{emb} r_{tot} dr \quad (4)$$

in which $E_{cluster}$ and E_{env} are the DFT energies of the cluster and environment in the presence of the embedding potential, V_{emb}. $\rho_{cluster}$ and ρ_{env} are the electron densities of the cluster and environment. The last term defines the interaction between the total electron density of the periodic slab, ρ_{tot}, and the embedding potential, V_{emb}. Maximizing the Wu-Yang functional yields

$$r_{cluster} + r_{env} = r_{tot}, \quad (5)$$

indicating that the summation of the electron density of the cluster and its environment equals the total electron density of the periodic slab at convergence.

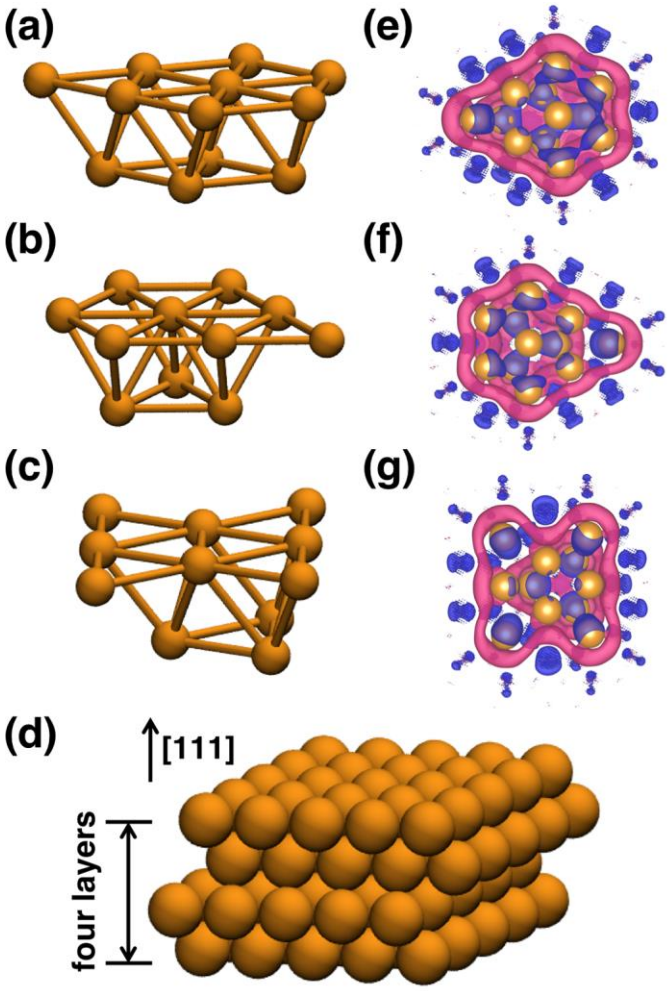

Figure 2. (a)-(c) display clusters used in ECW calculations, carved out from the periodic slab shown in (d). (a) Cu_{12} cluster for *CO adsorption. (b) Cu_{11} cluster for *H and *CHO adsorption and the CO reduction reaction to form *CHO. (c) Cu_{11} cluster for *COH adsorption and the CO reduction reaction to form *COH. (d) Four-layer 5×5 surface supercell Cu(111) periodic slab model. Isosurface plots (blue: +1 V, magenta: -1 V) of the embedding potentials generated for: (e) the Cu_{12} cluster in (a) and its Cu_{88} environment; (f) the Cu_{11} cluster in (b) and its Cu_{89} environment; (g) the Cu_{11} cluster in (c) and its Cu_{89} environment.

Embedded cluster calculations. We performed all embedded cluster calculations with Gaussian-type orbital (GTO) basis sets in MOLPRO[64,65] version 2012.1. The one-electron Hamiltonian (h^0) is modified as h^0+V_{emb} to include the interactions between the cluster and its environment via V_{emb} in the atomic orbital (AO) by calling the matrix operation feature in MOLPRO. The embedding integral matrices, $\langle AO|V_{emb}|AO\rangle$, were generated using our standalone embedding code, EmbeddingIntegralGenerator,[66] which is available on GitHub. We obtained the molecular geometries for the embedded cluster calculations by fixing the DFT-PBE-D3 optimized structures (internal coordinates) of the adsorbates on the periodic slab and

adding them onto the embedded clusters. The basis sets used were the all-electron aug-cc-pVDZ basis for C, H, and O,[67] as well as the cc-pVDZ basis for the valence electrons of Cu[68] accompanying effective core potentials (ECPs)[69] for the 10 core electrons.

The final ECW energy is evaluated as

$$E_{\mathrm{ECW}} = E_{\mathrm{slab}}^{\mathrm{DFT\text{-}PW}} + (E_{\mathrm{emb\text{-}cluster}}^{\mathrm{CW}} - E_{\mathrm{emb\text{-}cluster}}^{\mathrm{DFT}}) \quad (6)$$

in which $E_{\mathrm{slab}}^{\mathrm{DFT\text{-}PW}}$ is the plane-wave DFT total energy of the periodic slab (removing the D3 dispersion correction). $E_{\mathrm{emb\text{-}cluster}}^{\mathrm{CW}}$ and $E_{\mathrm{emb\text{-}cluster}}^{\mathrm{DFT}}$ are the energies of the embedded cluster respectively from correlated wavefunction (CW) theory and DFT in the presence of the embedding potential. We obtained $E_{\mathrm{emb\text{-}cluster}}^{\mathrm{DFT}}$ from spin-polarized DFT with the PBE XC functional. We computed $E_{\mathrm{emb\text{-}cluster}}^{\mathrm{CW}}$ via the embedded complete active space second-order perturbation theory (emb-CASPT2)[70,71] using reference wavefunctions generated by the embedded complete active space self-consistent field (emb-CASSCF)[72,73] method. The active space in emb-CASSCF calculations selected for the *CO adsorption site was (12e, 12o), *i.e.*, 12 electrons in 12 orbitals, including the C-O σ, σ* orbitals, two pairs of C-O π, π* orbitals, and three occupied and three unoccupied Cu 4*s*-derived orbitals on the Cu_{12} cluster (SI Figure S3). The active space used for the *H adsorption site was (12e, 12o), including the H-Cu σ, σ* orbitals and five occupied and five unoccupied Cu 4*s*-derived orbitals on the Cu_{11} cluster (SI Figure S4). The active space selected for the *CHO adsorption site was (12e, 12o), including the C-H σ, σ* orbitals, C-O σ, σ*, π, π* orbitals, C-Cu σ, σ*orbitals, 2*p* lone-pair electrons on the O atom and its correlating virtual orbital, and one occupied and one unoccupied Cu 4*s*-derived orbital on the Cu_{11} cluster (SI Figure S5). The active space used for *COH adsorption site also was (12e, 12o), including the O-H σ, σ* orbitals, C-O σ, σ* orbitals, three C-Cu σ, σ*orbitals, and one occupied and one unoccupied Cu 4*s*-derived orbital on the Cu_{11} cluster (SI Figure S6). The active space used for the CO reduction reaction to form *CHO was (16e, 14o), including the occupied C-O σ_{2s}, σ_{2s}* orbitals formed by C 2*s* and O 2*s* electrons, C-O σ, σ* orbitals, two pairs of C-O π, π* orbitals, H-Cu σ, σ* orbitals, and two occupied and two unoccupied Cu 4*s*-derived orbitals on the Cu_{11} cluster (SI Figure S7). The active space adopted to study the CO reduction reaction to form *COH was (14e, 14o), including the C-O σ, σ* orbitals, two pairs of C-O π, π* orbitals, H-Cu σ, σ* orbitals, two pairs of O-H σ, σ* orbitals on H_2O, and one occupied and one unoccupied Cu 4*s*-derived orbital on the Cu_{11} cluster (SI

Figure S8). In the emb-CASPT2 calculations, we included all single and double excitations from all electrons (excluding the 10 core electrons of each Cu subsumed into its ECP) to recover the dynamic correlation. We employed an "ionization potential electron affinity" (IPEA)[74] shift of 0.25 hartree to correct the error in the original formulation together with a level shift[75] of 0.3 hartree to aid convergence.

III. Results and discussion

Screening all possible adsorption sites for *CO, *H, *CHO, and *COH with ECW theory. We examined the four possible *CO adsorption sites on Cu(111): atop, bridge, hexagonal-close-packed (hcp) 3-fold hollow, and face-centered-cubic (fcc) 3-fold hollow sites (SI Figure S9). As expected, the theoretical predictions by DFT-PBE-D3 exhibit a preference for the fcc hollow-site adsorption, in disagreement with experimental observations of *CO atop-site adsorption[41,42] (Table 1). DFT-PBE-D3 predicts the most stable fcc hollow to be lower in energy by 0.14 eV than atop, with the other two adsites also predicted to be more stable by 0.12 eV (hcp hollow) and 0.10 eV (bridge) than the atop site. As mentioned above, pure DFT fails to properly situate the CO $2\pi^*$ level, with it being too low in energy, akin to DFT's well-known underestimation of band gaps. The too-low CO $2\pi^*$ level predicted by pure DFT enables spurious extra π-backbonding from the Cu surface, which favors hollow-site adsorption. By contrast, Sharifzadeh *et al.*[44] demonstrated that ECW theory recovers correctly the observed preference for *CO atop-site adsorption, because of the high-level treatment of exchange-correlation by ECW theory. Here, we again perform ECW calculations to revisit the *CO adsorption site. We used an even-numbered Cu cluster, Cu_{12}, to ensure an even number of total electrons, thus avoiding any spurious spin-polarization in the embedded cluster calculations (Figure 2a). The embedding potential optimized at the DFT-PBE-D3 level of theory by means of DFET[49-51] for the Cu_{12} cluster is shown in Figure 2e, with the magenta region representing the attractive bonding interaction between the cluster and its periodic slab environment. Consistent with the observations by Sharifzadeh *et al.*,[44] emb-CASPT2 correctly reproduces the experimental observation of atop-site adsorption of *CO, which is more stable by ~0.2 eV compared to any other adsite, suggesting that emb-CASPT2 using reference wavefunctions generated by emb-CASSCF is a suitable approach to study CO_2 reduction on Cu.

Table 1. Relative energies (eV) for atop-, bridge-, fcc hollow-, hcp hollow-, and (for CHO only) bidentate atop-site adsorption of each adsorbate on Cu(111), referenced against the preferred emb-CASPT2 adsite, evaluated by DFT-PBE-D3 and emb-CASPT2 methods.

		atop	bridge	fcc	hcp	bidentate atop
*CO	DFT-PBE-D3	0.00	-0.10	-0.14	-0.12	
	emb-CASPT2	0.00	0.18	0.20	0.18	
H*	DFT-PBE-D3	0.63	0.14	0.00	0.00	
	emb-CASPT2	0.51	0.20	0.00	0.01	
*CHO	DFT-PBE-D3	0.08	0.02	0.10	0.11	0.00
	emb-CASPT2	0.22	0.13	0.47	0.66	0.00
*COH	DFT-PBE-D3	1.22	0.11	-0.04	0.00	
	emb-CASPT2	2.47	0.07	0.09	0.00	

The same four possible *H adsites on Cu(111) are compared (SI Figure S10), again by means of periodic DFT-PBE-D3 and emb-CASPT2 calculations. Using a Cu_{11} cluster to ensure an even number of total electrons upon H adsorption and its corresponding optimized embedding potential (Figure 2b, 2f), emb-CASPT2 predicts that fcc and hcp hollow-site adsorption for *H are essentially equally preferred, consistent with DFT-PBE-D3 predictions (Table 1). The emb-CASSCF calculations employ an active space of (12e,12o), including the Cu-H σ, σ^* orbitals and all other Cu 4*s*-derived orbitals (five occupied and five unoccupied) on the Cu_{11} cluster. This system was used to determine the minimum number of Cu 4*s*-derived orbitals that need to be correlated in the active space to produce similar results as the full active space. We observed the same preference for fcc and hcp hollow adsorption and the same relative stabilities for the four different *H adsorption sites even when reducing the active space to (4e,4o), comprised of the Cu-H σ, σ^* orbitals and only two Cu 4*s*-derived orbitals, indicating that chemical accuracy can still be maintained when reducing the number of Cu 4*s*-derived orbitals in the active space to two, as will be needed for complicated adsorbates (SI Table S1).

We next investigate adsorption of *CHO, a possible intermediate in CO reduction on Cu(111). In addition to the four possible adsites listed above, *CHO also has been proposed[26,76] to reside on top of two adjacent Cu atoms with the C-O bond nearly parallel to the Cu-Cu bond, forming a dative bond from an O lone pair to the Cu surface, denoted as a bidentate atop site (SI Figure S11). DFT-PBE-D3 predicts that bidentate atop-site adsorption of *CHO is preferred (Table 1). Emb-CASPT2, using the same Cu_{11} cluster as for modeling *H adsorption and its optimized embedding potential, also favors the bidentate atop site. Although both DFT-PBE-D3 and emb-CASPT2 predict the same site preference for *CHO, emb-CASPT2 more strongly

favors the bidentate atop site whereas DFT-PBE-D3 only weakly prefers it, with all other adsites within ~0.1 eV higher (Table 1). This very weak preference of the bidentate atop site by DFT probably explains why a plethora of mechanisms have been proposed that begin with a diverse set of *CHO adsites, including atop,[18,19,27,76] bidentate atop,[26,76] and bridge,[17,22,24] although other modeling parameters (e.g., Cu surface facet, treatment of solvation) also may affect site preferences.

Adsorption of *COH, the other proposed intermediate in the first step of CO reduction on Cu(111), again could involve any of the same four adsites (SI Figure S12). DFT-PBE-D3 favors the fcc hollow but only by 0.04 eV compared to the hcp hollow (Table 1). However, using the Cu_{11} cluster and its optimized embedding potential shown in Figure 2b and 2f, emb-CASPT2 predicts an unphysically large energy difference (2.12 eV) between fcc versus hcp hollow-site adsorption of *COH. This unreasonable energy difference originates from an edge artifact on this cluster when modeling the *COH fcc hollow-site adsorption on the Cu_{11} cluster shown in Figure 2b. The edge effect leads to inevitable inclusion of the Cu 3*d* orbital character in the active space of the emb-CASSCF calculations and results in unstable fcc hollow-site adsorption (SI Figures S13, S14). Switching to the Cu_{11} cluster shown in Figure 2c, which eliminates the edge effect for both fcc and hcp hollow-site adsorption (SI Figures S12, S13) and its optimized embedding potential (Figure 2g), emb-CASPT2 predicts that the most stable adsite for *COH is the hcp hollow but the bridge and fcc hollow sites are accessible as well, at less than 0.1 eV higher in energy. Thus, DFT-PBE-D3 and emb-CASPT2 favor different hollow sites – fcc and hcp respectively – as absolute minima for *COH adsorption, although the magnitude difference is within our margin of error.

*CO + *H → *CHO reaction pathway with ECW theory. With the adsorption sites identified with emb-CASPT2, we next examine with ECW theory one of the possible first steps in CO reduction, namely formation of *CHO on Cu(111). We consider here the reaction proceeding via a surface *H transfer step through direct hydrogenation by an adsorbed *H species. Previously, Nie *et al.*[19] predicted a DFT-PBE barrier for *CHO formation on Cu(111) by *H transfer to *CO of 1.03 eV including the zero-point energy (ZPE) corrections; including one explicit water molecule to stabilize *CO and *CHO reduces the barrier by less than 0.05 eV. Given the small effect of a solvating water molecule on this reaction, we did not include one here. Starting from the preferred adsorption sites of *CO, *H, and *CHO predicted by ECW

theory, we then determined the MEP at the DFT-PBE-D3 level of theory under the constraint of fixed new initial structures. Figure 3a displays the critical structures along the reaction path (all MEP structures can be found in Figure S1 in the SI). Initially, the CO molecule chemisorbs at an atop site, and the H atom chemisorbs at a nearby fcc hollow site. The H atom then moves toward the CO molecule, while the CO molecule moves away from the initial atop site to an adjacent bridge site, which is more stable at the DFT-PBE-D3 level. At the transition state, the CO molecule moves back to the original atop site and the C-H bond forms. After that, the CHO reorients toward the most stable bidentate atop adsorption site. The DFT-PBE-D3 barrier for C-H bond formation is 1.13 eV; with DFT-PBE-D3 ZPE corrections, the barrier decreases slightly to 1.05 eV. This is comparable to the barrier of 1.03 eV reported by Nie *et al.*,[19] though via different *CHO adsites, *i.e.*, bidentate atop here (Figure 3a) versus atop in Nie *et al.*'s work.

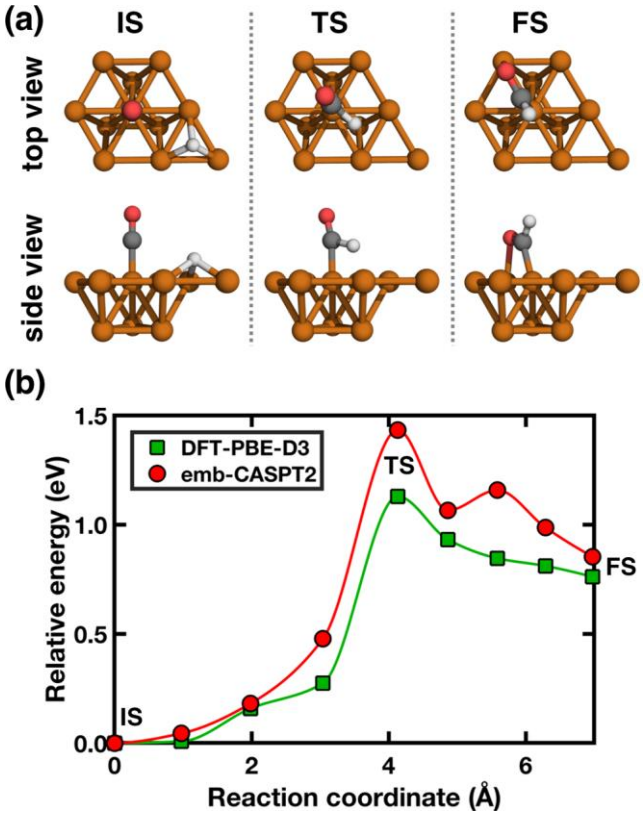

Figure 3. (a) Initial state (IS), transition state (TS), and final state (FS) structures (top and side views) optimized by DFT-PBE-D3 along the MEPs starting from preferred ECW-predicted adsorption sites for the reactants in CO reduction to form *CHO on Cu(111). Atoms are colored as follows: Cu in brown, C in dark gray, O in red, and H in light gray. The same color scheme is used in all figures. Only the Cu_{11} fragments of the slabs are shown; the ECW calculations use this same Cu_{11} cluster. (b) Energy curves along the MEP for CO reduction to form *CHO on Cu(111), predicted by DFT-PBE-D3 (green squares) and emb-CASPT2 (red circles).

When performing ECW calculations to correct the energetics at each interpolated structure along the MEP for *CHO formation, we use an active space of (16e, 14o) in the emb-CASSCF calculations, including the occupied C-O σ_{2s}, σ_{2s}* orbitals, C-O σ, σ* orbitals, two pairs of C-O π, π* orbitals, H-Cu σ, σ* orbitals, and four Cu 4*s*-derived orbitals (two occupied and two unoccupied) on the Cu_{11} cluster (SI Figure S7). Using the reaction path predicted by DFT-PBE-D3 and the Cu_{11} cluster and its optimized embedding potential shown in Figure 2b and 2f, our emb-CASPT2 calculations with this (16e, 14o) active space yield a C-H bond formation barrier of 1.43 eV (1.35 eV after adding DFT-PBE-D3 ZPE corrections), 0.3 eV higher than the DFT-PBE-D3 barrier (Figure 3b). Beyond the differing reaction barriers predicted by the two theories, the emb-CASPT2 energy curve exhibits a local minimum at structure (image) five along the MEP, unlike the DFT-PBE-D3 energy curve (Figure 3 and SI Figure S1). At image five, the *CHO resides in an atop site with its C-H bond nearly parallel to the Cu surface while at image 6, the atop *CHO has the C-H bond pointed toward vacuum. The inclusion of high-level electron correlation – a superior description of dispersion – via CASPT2 theory stabilizes the non-bonded interaction of the C-H bond with the surface, producing the local minimum.

When simulating the reaction pathway for *COH formation, we include one explicit water molecule in a water-assisted H-shuttling model (*vide infra*), necessitating inclusion of four additional electrons and orbitals (σ, σ, σ*, σ*) from the two O-H bonds of the water molecule, in addition to the 16 electrons and 14 orbitals for the reaction of *H with *CO. This active space of (20e, 18o) to model *COH formation is prohibitively expensive for both emb-CASSCF and emb-CASPT2. Thus, to have a consistent active space across the two CO reduction reactions (to form either *CHO or *COH), the minimum active space size that still delivers accurate barriers needs to be determined so that unnecessary orbitals may be eliminated from the active space of the *CHO reaction pathway. We first reduced the active space from (16e, 14o) to (12e, 12o) by eliminating the low-energy occupied C-O σ_{2s}, σ_{2s}* orbitals for the *CHO reaction pathway. This increases the emb-CASPT2 barrier slightly to 1.46 eV and slightly decreases the emb-CASPT2 reaction energy to 0.83 eV, within 0.03 eV of results using the original benchmark active space of (16e, 14o) (Table 2 and SI Figure S15). We then investigated the number of Cu 4*s*-derived orbitals needed in the active space. Reducing the number of Cu 4*s*-derived orbitals and electrons from four to two, giving an active space of (14e,

12o), increases the barrier to 1.50 eV and the reaction energy to 0.91 eV, still close to the benchmark (Table 2 and SI Figure S15). Further elimination of all Cu 4*s*-derived orbitals to an active space of (12e, 10o) significantly altered both the barrier and reaction energy to 1.83 eV and 1.21 eV, respectively, indicating the necessity of correlating at least two Cu 4*s*-derived orbitals in the active space (Table 2, SI Figure S15). Based on these results, we simultaneously eliminate the C-O σ_{2s}, σ_{2s}* orbitals and keep only two Cu 4*s*-derived orbitals to form an active space of (10e, 10o), including the C-O σ, σ* orbitals, two pairs of C-O π, π* orbitals, H-Cu σ, σ* orbitals, and two Cu 4*s*-derived orbitals. This active space produces an emb-CASPT2 barrier of 1.53 eV and reaction energy of 0.88 eV, which achieves our conventional accuracy target of being within 0.1 eV compared with the largest active space results (Table 2 and SI Figure S15). The similar energetics obtained using this smaller active space of (10e, 10o) for the *CHO formation indicates that a comparable active space of (14e, 14o) with four additional σ, σ, σ*, σ* orbitals and electrons from the two O-H bonds of the water molecule can be used to model accurately the *COH reaction pathway instead of the prohibitively expensive one of (20e, 18o). We use this (14e, 14o) active space below.

Table 2. Activation barriers (E_a) and reaction energies (ΔE) for the *CHO pathway predicted by emb-CASPT2 using different active spaces, and orbital identities for each active space: the number of Cu 4*s*-derived orbitals (# Cu 4*s*) included in the active space and inclusion (or not) of C-O σ_{2s} and σ_{2s}* orbitals (σ_{2s}, σ_{2s}*).

active space	E_a (eV)	ΔE (eV)	# Cu 4*s*	σ_{2s}, σ_{2s}*
(16e,14o)	1.43	0.85	4	yes
(14e,12o)	1.50	0.91	2	yes
(12e,10o)	1.83	1.21	0	yes
(12e,12o)	1.46	0.83	4	no
(10e,10o)	1.53	0.88	2	no

*CO + *H + H_2O → *COH + H_2O reaction pathway with ECW theory. We consider here the other possible CO reduction reaction pathway of forming *COH instead of *CHO on Cu(111). Previously, Nie *et al.*[18,19] used DFT-PBE to predict that the barriers for O-H bond formation steps in the CO_2RR on Cu(111) can be lowered dramatically via a water-assisted H-shuttling mechanism, in which simultaneously an *H transfers to a solvent water molecule while another H atom in that water molecule transfers to the adsorbate. For example, they reported[19] that the barrier decreases from 1.43 to 0.76 eV via the water-assisted H-shuttling mechanism

for the *COOH reduction step to form *CO. Given this large effect on the kinetics, we only consider the water-assisted H-shuttling mechanism for the *COH formation pathway and therefore add one explicit water molecule in our calculations. As in the other reduction step, we start from the preferred adsites of *CO, *H, and *COH predicted by ECW theory to optimize the MEP at the DFT-PBE-D3 level of theory. Initially, the *CO chemisorbs at an atop site, the *H chemisorbs at a nearby hcp hollow site, and the H_2O molecule is 3.6 Å away from the Cu surface, as shown in Figure 4a and SI Figure S2. *H then moves to an adjacent bridge site, the H_2O molecule slightly moves and reorients above *H, and *CO moves to an adjacent bridge site. At the transition state, the initially adsorbed *H leaves the surface and its electron behind, effectively transferring as a proton to the H_2O to form a transient hydronium ion, and the *CO moves toward an hcp hollow site to approach the hydronium ion. After that, a different proton originally from the H_2O molecule transfers to *CO to form *COH adsorbed in an hcp hollow with the H hydrogen-bonded to the O in the water molecule (Figure 4a and SI Figure S2). DFT-PBE-D3 predicts an activation barrier of 0.58 eV and, with ZPE corrections, yields a barrier of 0.51 eV for *COH formation. This barrier is roughly half the DFT-PBE-D3 barrier to form *CHO, suggesting that the first step in CO reduction on Cu(111) is to form *COH instead of *CHO (Figure 4b). The preference for the *COH pathway is consistent with the predictions of Nie *et al.*,[18,19] although they reported a slightly higher *COH formation barrier of 0.71 eV, originating from a different proposed reaction pathway that formed *COH adsorbed at an fcc hollow instead of the ECW-favored hcp hollow.

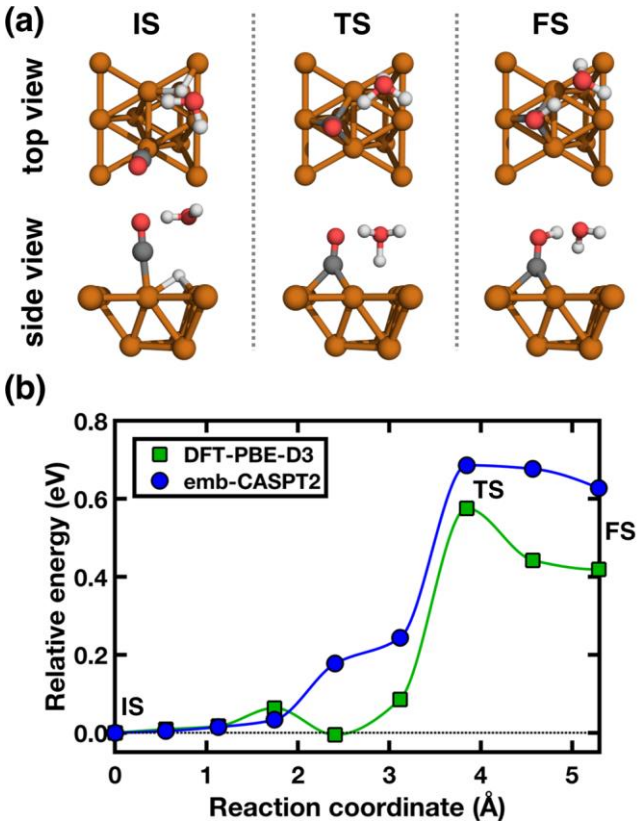

Figure 4. (a) Initial state (IS), transition state (TS), and final state (FS) structures (top and side views) optimized by DFT-PBE-D3 along the MEPs starting from the preferred ECW-predicted adsorption sites for the reactants in CO reduction to form *COH on Cu(111). Only the Cu_{11} fragments of the slabs are shown; the ECW calculations use this same Cu_{11} cluster. (b) Energy curves along the MEP for CO reduction to form *COH on Cu(111), predicted by DFT-PBE-D3 (green squares) and emb-CASPT2 (blue circles).

We then use ECW theory to re-evaluate the *COH formation barrier on Cu(111). For the same DFT-PBE-D3 reaction pathway, emb-CASPT2 predicts an activation barrier of 0.69 eV (0.62 eV including DFT-PBE-D3 ZPE corrections) using the Cu_{11} cluster and its optimized embedding potential shown in Figure 2c and 2g, which is only 0.11 eV higher than the DFT-PBE-D3 barrier. Note the local minimum at structure (image) four along the DFT-PBE-D3 MEP in which the *CO migrates to a bridge site (Figure 4 and SI Figure S2). This occurs because DFT incorrectly favors *CO bridge-site adsorption over atop-site adsorption, resulting in a spurious local minimum while ECW theory removes this error.

The emb-CASPT2 evaluations of the *CHO and *COH formation pathways provide rigorous confirmation that the first step in CO reduction on Cu(111) is to form *COH instead of *CHO. Emb-CASPT2 reaction energies indicate that *COH formation is favored over *CHO

formation by 0.25 eV (0.63 eV for *COH versus 0.88 eV for *CHO) when using comparable active spaces for the two reactions, *i.e.*, (10e, 10o) for *CHO formation and (14e, 14o) for *COH formation, in the ECW calculations (Figure 5). Kinetics as predicted by emb-CASPT2 further enhances the preference for the *COH path: the *COH formation barrier (0.69 eV) is 0.84 eV lower than the *CHO formation barrier (1.53 eV). A larger active space of (16e, 14o) does decrease further the emb-CASPT2 *CHO formation barrier (1.43 eV) and reaction energy (0.85 eV) but not enough to make it competitive with *COH formation.

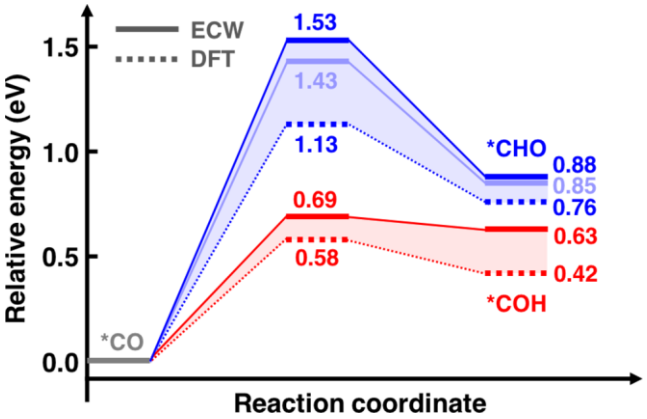

Figure 5. Energetics of the CO reduction reaction on Cu(111) to form *CHO (blue lines) and *COH (red lines) predicted by DFT-PBE-D3 (dashed lines) and emb-CASPT2 (solid lines). Energetics of the *CHO pathway predicted by emb-CASPT2 are shown for two different active spaces: (16e, 14o) (light blue solid lines) and (10e, 10o) (blue solid lines).

Although DFT-PBE-D3 consistently favors *COH over *CHO formation both thermodynamically and kinetically, DFT-PBE-D3 predicts a slightly larger reaction energy difference (0.34 eV) and a smaller activation barrier difference (0.55 eV) between the two reactions compared to the emb-CASPT2 energy differences. Moreover, the two theories predict quite different structural and mechanistic behaviors, *e.g.*, the local minimum in the emb-CASPT2 energy curve for *CHO formation caused by stabilization of a particular orientation of the C-H bond (C-H bond parallel to the Cu surface in a quasi-atop site at image 5 versus C-H bond pointed toward vacuum in a classic atop site at image 6), as well as the local minimum in the DFT-PBE-D3 energy curve for *COH formation because of the incorrect preference for bridge-site adsorption of *CO at the DFT-PBE-D3 level of theory. These artifacts in the structure and energetics predicted by DFT-PBE-D3 motivate verification of other parts of the mechanisms that have been proposed for CO_2RR on Cu surfaces based on DFT approximations.

All calculations discussed thus far neglected consideration of solvation effects. For completeness, we tested the effect of an implicit (continuum) solvation model[77,78] on DFT-PBE-D3 activation barriers and reaction energies for *CHO and *COH formation via hydrogen transfer. Implicit solvation alters the energetics by no more than 0.05 eV (SI Table S2). To further understand this result, we assessed the polarity of the adsorbates in vacuum and solvated by performing Bader charge analysis[79,80] (SI Table S3). We observe very little difference in the polarity of the species in vacuum and with implicit solvation in their initial and transition states for both the *CHO and *COH pathways, thus explaining the very minor alteration in reaction energetics upon solvation of these species.

In addition to the potential effects of solvent, varying reactant surface coverages could affect the energetics as well. DFT calculations by Montoya *et al.*[81] and Huang *et al.*[82] led to the prediction that a high *CO coverage may reduce the barrier to C_2H_4 formation via dimerization of two *CO. By contrast, we anticipate *H transfer barriers to *CO will not be very sensitive to *CO coverage, unlike a dimerization pathway involving two *CO. However, the exact effect of reactant coverage on the barriers of competing steps in electrochemical CO_2RR on Cu at the ECW level of theory needs to be the subject of future work.

Note that the reduction of *CO to *COH on Cu(111) studied here assumes an *H transfer mechanism via interaction of *CO with adsorbed *H. We are currently exploring alternative pathways involving PCET via interaction with water molecules. Although the CO_2RR on Cu is an electrochemical reaction overall, the two CO reduction steps considered here are simply chemical – rather than electrochemical – reactions since no electrons transfer. The energetics therefore will not change with applied potential and thus potential-dependent barriers and reaction energies need not be considered whereas the electrochemical CO reduction through a PCET path will be affected by applied potential and therefore potentially could be more favorable.

IV. Conclusions

Motivated by the incorrect prediction by standard DFAs of the preferred adsorption site on metal surfaces for *CO, an important intermediate in electrochemical CO_2 reduction, we re-evaluated a key mechanistic component of CO_2 reduction on Cu(111) using a higher level of theory, namely ECW theory, which corrects the XC error in DFAs in the region of interest.

Previous experiments indicate that the rate-limiting step in electrochemical CO_2 reduction is CO reduction, based on the similar products and overpotentials yielded from these two reactions. We therefore focused on examining the CO reduction step in this work. We compared the kinetics of CO reduction to form *CHO versus *COH on Cu(111) via a surface *H transfer mechanism. We first screened all possible adsorption sites for each adsorbate with ECW theory. In contrast to the incorrect hollow-site adsorption of *CO predicted by DFT-PBE-D3, emb-CASPT2 correctly retrieves the experimental atop-site ground state, indicating that it is an appropriate approach to study CO_2 reduction. For the *H adsorption site, emb-CASPT2 yielded equally stable fcc and hcp hollow sites, consistent with DFT-PBE-D3 calculations. Although both emb-CASPT2 and DFT-PBE-D3 favor the bidentate atop-site for *CHO adsorption, emb-CASPT2 exhibits a relatively strong preference whereas DFT-PBE-D3 only predicted a weak preference over other adsorption sites. For *COH adsorption, both theories favor hollow-sites with both hcp and fcc exhibiting nearly equal stability within our 0.1 eV margin of error.

Given the fact that optimizing reaction pathways directly with emb-CASPT2 is not possible, we instead optimized the CO reduction reaction pathways to form *CHO and *COH at the DFT-PBE-D3 level of theory starting from these ECW theory preferred adsorption sites as initial constraints and then corrected the energetics at each interpolated structure along the reaction pathways with ECW theory. For the *CHO formation pathway, the barrier was estimated to be 1.13 eV at the DFT-PBE-D3 level versus 1.43 eV (1.53 eV) at the emb-CASPT2 level, within a (16e, 14o) ((10e, 10o)) active space. Beyond the differing barriers predicted by the two theories, we observed a local minimum in the emb-CASPT2 energy curve caused by stabilization of a particular orientation of the C-H bond (parallel to the Cu(111) surface) not captured by DFT-PBE-D3. For the *COH formation pathway, DFT-PBE-D3 yielded a barrier of 0.58 eV while emb-CASPT2 predicted an only slightly higher barrier of 0.69 eV based on a (14e, 14o) active space. The two theories again exhibited different minimum energy path characteristics, in that a local minimum appears in the DFT-PBE-D3 energy curve due to an incorrect preference for bridge-site over atop-site adsorption of *CO.

Thus, comparing the ECW barriers for the two different pathways, we rigorously confirmed that the first step in CO reduction on Cu(111) involves *COH instead of *CHO formation, via a surface *H transfer mechanism, with *COH formation kinetically preferred over *CHO formation by 0.84 eV. However, alternative paths through PCET steps via interaction

with water molecules might be more favorable under applied potential and thus such paths are being explored with ECW theory in ongoing work.

Supporting Information

Complete sets of geometries along the MEPs for CO reduction to form *CHO and *COH; natural orbitals of the emb-CASSCF active spaces for *CO, *H, *CHO, and *COH adsorption; natural orbitals of the emb-CASSCF active spaces for CO reduction to form *CHO and *COH; geometries of *CO, *H, *CHO, and *COH adsorption sites; different Cu_{11} clusters and orbitals for *COH adsorption; emb-CASPT2 energy curves for *CHO formation; stabilities of *H adsorption sites by emb-CASPT2, activation barriers and reaction energies with implicit solvation, and Bader charge analysis of adsorbates in vacuum and solvated. (PDF)

Corresponding Author

*eac@princeton.edu, eac@ ucla.edu

Notes

The authors declare no competing financial interests.

Acknowledgements

This work was supported as part of the Advanced Scientific Computing Research Program funded by the U.S. Department of Energy, Office of Science, Basic Energy Sciences, under Award # DE-AC02-05CH11231. This work was carried out using computational resources from Princeton University's Terascale Infrastructure for Groundbreaking Research in Engineering and Science (TIGRESS). The authors thank Dr. Junwei Lucas Bao, Dr. Shenzhen Xu, and Dr. John Mark P. Martirez for insightful discussions, and Ms. Nari Baughman and Ms. Samantha Luu for providing a critical reading and careful editing of the manuscript.

References

1. Hori, Y. Electrochemical CO_2 Reduction on Metal Electrodes. In *Modern Aspects of Electrochemistry*, Vayenas, C. G.; White, R. E.; Gamboa-Aldeco, M. E., Eds.; Springer: New York, NY, 2008; pp 89-189.
2. Kondratenko, E. V.; Mul, G.; Baltrusaitis, J.; Larrazábal, G. O.; Pérez-Ramírez, J. Status and Perspectives of CO_2 Conversion into Fuels and Chemicals by Catalytic, Photocatalytic and Electrocatalytic Processes. *Energy Environ. Sci.* **2013**, *6*, 3112-3135.
3. Otto, A.; Grube, T.; Schiebahn, S.; Stolten, D. Closing the Loop: Captured CO_2 as a Feedstock in the Chemical Industry. *Energy Environ. Sci.* **2015**, *8*, 3283-3297.
4. Xu, S.; Carter, E. A. Theoretical Insights into Heterogeneous (Photo)Electrochemical CO_2 Reduction. *Chem. Rev.* **2018**, *119*, 6631-6669.
5. Hori, Y.; Kikuchi, K.; Suzuki, S. Production of CO and CH_4 in Electrochemical Reduction of CO_2 at Metal Electrodes in Aqueous Hydrogencarbonate Solution. *Chem. Lett.* **1985**, *14*, 1695-1698.
6. Hori, Y.; Kikuchi, K.; Murata, A.; Suzuki, S. Production of Methane and Ethylene in Electrochemical Reduction of Carbon Dioxide at Copper Electrode in Aqueous Hydrogencarbonate Solution. *Chem. Lett.* **1986**, *15*, 897-898.
7. Hori, Y.; Murata, A.; Takahashi, R. Formation of Hydrocarbons in the Electrochemical Reduction of Carbon Dioxide at a Copper Electrode in Aqueous Solution. *J. Chem. Soc. Faraday Trans.* **1989**, *85*, 2309-2326.
8. Hori, Y.; Wakebe, H.; Tsukamoto, T.; Koga, O. Electrocatalytic Process of CO Selectivity in Electrochemical Reduction of CO_2 at Metal Electrodes in Aqueous Media. *Electrochim. Acta* **1994**, *39*, 1833-1839.
9. Hara, K.; Kudo, A.; Sakata, T. Electrochemical Reduction of Carbon Dioxide under High Pressure on Various Electrodes in an Aqueous Electrolyte. *J. Electroanal. Chem.* **1995**, *391*, 141-147.
10. Jitaru, M.; Lowy, D. A.; Toma, M.; Toma, B. C.; Oniciu, L. Electrochemical Reduction of Carbon Dioxide on Flat Metallic Cathodes. *J. Appl. Electrochem.* **1997**, *27*, 875-889.
11. Schouten, K. J. P.; Kwon, Y.; Van der Ham, C. J. M.; Qin, Z.; Koper, M. T. M. A New Mechanism for the Selectivity to C_1 and C_2 Species in the Electrochemical Reduction of Carbon Dioxide on Copper Electrodes. *Chem. Sci.* **2011**, *2*, 1902-1909.
12. Kuhl, K. P.; Cave, E. R.; Abram, D. N.; Jaramillo, T. F. New Insights into the Electrochemical Reduction of Carbon Dioxide on Metallic Copper Surfaces. *Energy Environ. Sci.* **2012**, *5*, 7050-7059.
13. Hori, Y.; Takahashi, I.; Koga, O.; Hoshi, N. Electrochemical Reduction of Carbon Dioxide at Various Series of Copper Single Crystal Electrodes. *J. Mol. Catal. Chem.* **2003**, *199*, 39-47.
14. Schouten, K. J. P.; Qin, Z.; Pérez Gallent, E.; Koper, M. T. M. Two Pathways for the Formation of Ethylene in CO Reduction on Single-Crystal Copper Electrodes. *J. Am. Chem. Soc* **2012**, *134*, 9864-9867.
15. Schouten, K. J. P.; Gallent, E. P.; Koper, M. T. M. The Influence of pH on the Reduction of CO and CO_2 to Hydrocarbons on Copper Electrodes. *J. Electroanal. Chem.* **2014**, *716*, 53-57.
16. Hori, Y.; Takahashi, R.; Yoshinami, Y.; Murata, A. Electrochemical Reduction of CO at a Copper Electrode. *J. Phys. Chem. B* **1997**, *101*, 7075-7081.

17. Peterson, A. A.; Abild-Pedersen, F.; Studt, F.; Rossmeisl, J.; Nørskov, J. K. How Copper Catalyzes the Electroreduction of Carbon Dioxide into Hydrocarbon Fuels. *Energy Environ. Sci.* **2010**, *3*, 1311-1315.
18. Nie, X.; Esopi, M. R.; Janik, M. J.; Asthagiri, A. Selectivity of CO_2 Reduction on Copper Electrodes: The Role of the Kinetics of Elementary Steps. *Angew. Chem.* **2013**, *52*, 2459-2462.
19. Nie, X.; Luo, W.; Janik, M. J.; Asthagiri, A. Reaction Mechanisms of CO_2 Electrochemical Reduction on Cu(111) Determined with Density Functional Theory. *J. Catal.* **2014**, *312*, 108-122.
20. Xiao, H.; Cheng, T.; Goddard III, W. A.; Sundararaman, R. Mechanistic Explanation of the pH Dependence and Onset Potentials for Hydrocarbon Products from Electrochemical Reduction of CO on Cu(111). *J. Am. Chem. Soc* **2016**, *138*, 483-486.
21. Xiao, H.; Cheng, T.; Goddard III, W. A. Atomistic Mechanisms Underlying Selectivities in C_1 and C_2 Products from Electrochemical Reduction of CO on Cu(111). *J. Am. Chem. Soc* **2017**, *139*, 130-136.
22. Cheng, T.; Xiao, H.; Goddard III, W. A. Free-Energy Barriers and Reaction Mechanisms for the Electrochemical Reduction of CO on the Cu(100) Surface, Including Multiple Layers of Explicit Solvent at pH 0. *J. Phys. Chem. Lett.* **2015**, *6*, 4767-4773.
23. Goodpaster, J. D.; Bell, A. T.; Head-Gordon, M. Identification of Possible Pathways for C–C Bond Formation During Electrochemical Reduction of CO_2: New Theoretical Insights from an Improved Electrochemical Model. *J. Phys. Chem. Lett.* **2016**, *7*, 1471-1477.
24. Cheng, T.; Xiao, H.; Goddard, W. A. Full Atomistic Reaction Mechanism with Kinetics for CO Reduction on Cu(100) from Ab Initio Molecular Dynamics Free-Energy Calculations at 298k. *Proc. Natl. Acad. Sci.* **2017**, *114*, 1795-1800.
25. Garza, A. J.; Bell, A. T.; Head-Gordon, M. Mechanism of CO_2 Reduction at Copper Surfaces: Pathways to C_2 Products. *ACS Catal.* **2018**, *8*, 1490-1499.
26. Shi, C.; Chan, K.; Yoo, J. S.; Nørskov, J. K. Barriers of Electrochemical CO_2 Reduction on Transition Metals. *Org. Process Res. Dev.* **2016**, *20*, 1424-1430.
27. Liu, X.; Xiao, J.; Peng, H.; Hong, X.; Chan, K.; Nørskov, J. K. Understanding Trends in Electrochemical Carbon Dioxide Reduction Rates. *Nat. Commun.* **2017**, *8*, 15438.
28. Mori-Sánchez, P.; Cohen, A. J.; Yang, W. Many-Electron Self-Interaction Error in Approximate Density Functionals. *J. Chem. Phys.* **2006**, *125*, 201102.
29. Cohen, A. J.; Mori-Sánchez, P.; Yang, W. Insights into Current Limitations of Density Functional Theory. *Science* **2008**, *321*, 792-794.
30. Feibelman, P. J.; Hammer, B.; Nørskov, J. K.; Wagner, F.; Scheffler, M.; Stumpf, R.; Watwe, R.; Dumesic, J. The CO/Pt (111) Puzzle. *J. Phys. Chem. B* **2001**, *105*, 4018-4025.
31. Wellendorff, J.; Silbaugh, T. L.; Garcia-Pintos, D.; Nørskov, J. K.; Bligaard, T.; Studt, F.; Campbell, C. T. A Benchmark Database for Adsorption Bond Energies to Transition Metal Surfaces and Comparison to Selected DFT Functionals. *Surf. Sci.* **2015**, *640*, 36-44.
32. Sharada, S. M.; Bligaard, T.; Luntz, A. C.; Kroes, G.-J.; Nørskov, J. K. SBH10: A Benchmark Database of Barrier Heights on Transition Metal Surfaces. *J. Phys. Chem. C* **2017**, *121*, 19807-19815.
33. Zhao, Q.; Kulik, H. J. Stable Surfaces That Bind Too Tightly: Can Range-Separated Hybrids or DFT+U Improve Paradoxical Descriptions of Surface Chemistry? *J. Phys. Chem. Lett.* **2019**, *10*, 5090-5098.
34. Perdew, J. P.; Burke, K.; Ernzerhof, M. Generalized Gradient Approximation Made Simple. *Phys. Rev. Lett.* **1996**, *77*, 3865.

35. Hammer, B.; Hansen, L. B.; Nørskov, J. K. Improved Adsorption Energetics within Density-Functional Theory Using Revised Perdew-Burke-Ernzerhof Functionals. *Phys. Rev. B* **1999**, *59*, 7413.
36. Wellendorff, J.; Lundgaard, K. T.; Møgelhøj, A.; Petzold, V.; Landis, D. D.; Nørskov, J. K.; Bligaard, T.; Jacobsen, K. W. Density Functionals for Surface Science: Exchange-Correlation Model Development with Bayesian Error Estimation. *Phys. Rev. B* **2012**, *85*, 235149.
37. Gajdoš, M.; Eichler, A.; Hafner, J. CO Adsorption on Close-Packed Transition and Noble Metal Surfaces: Trends from Ab Initio Calculations. *J. Phys. Condens. Matter* **2004**, *16*, 1141.
38. Neef, M.; Doll, K. CO Adsorption on the Cu(111) Surface: A Density Functional Study. *Surf. Sci.* **2006**, *600*, 1085-1092.
39. Luo, S.; Zhao, Y.; Truhlar, D. G. Improved CO Adsorption Energies, Site Preferences, and Surface Formation Energies from a Meta-Generalized Gradient Approximation Exchange–Correlation Functional, M06-L. *J. Phys. Chem. Lett.* **2012**, *3*, 2975-2979.
40. Kundappaden, I.; Chatanathodi, R. A DFT Study of CO Adsorption on Pt(111) Using Van Der Waals Functionals. *Surf. Sci.* **2019**, *681*, 143-148.
41. Raval, R.; Parker, S. F.; Pemble, M. E.; Hollins, P.; Pritchard, J.; Chesters, M. A. FT-RAIRS, EELS and LEED Studies of the Adsorption of Carbon Monoxide on Cu(111). *Surf. Sci.* **1988**, *203*, 353-377.
42. Vollmer, S.; Witte, G.; Wöll, C. Determination of Site Specific Adsorption Energies of CO on Copper. *Catal. Lett.* **2001**, *77*, 97-101.
43. Doll, K. Co Adsorption on the Pt(111) Surface: A Comparison of a Gradient Corrected Functional and a Hybrid Functional. *Surf. Sci.* **2004**, *573*, 464-473.
44. Sharifzadeh, S.; Huang, P.; Carter, E. A. Embedded Configuration Interaction Description of CO on Cu(111): Resolution of the Site Preference Conundrum. *J. Phys. Chem. C* **2008**, *112*, 4649-4657.
45. Wang, Y.; de Gironcoli, S.; Hush, N. S.; Reimers, J. R. Successful a Priori Modeling of CO Adsorption on Pt(111) Using Periodic Hybrid Density Functional Theory. *J. Am. Chem. Soc* **2007**, *129*, 10402-10407.
46. Stroppa, A.; Termentzidis, K.; Paier, J.; Kresse, G.; Hafner, J. CO Adsorption on Metal Surfaces: A Hybrid Functional Study with Plane-Wave Basis Set. *Phys. Rev. B* **2007**, *76*, 195440.
47. Lazić, P.; Alaei, M.; Atodiresei, N.; Caciuc, V.; Brako, R.; Blügel, S. Density Functional Theory with Nonlocal Correlation: A Key to the Solution of the CO Adsorption Puzzle. *Phys. Rev. B* **2010**, *81*, 045401.
48. Ashcroft, N. W.; Mermin, N. D. *Solid State Physics*. Holt, Rinehart and Winston: New York, 1976.
49. Huang, C.; Pavone, M.; Carter, E. A. Quantum Mechanical Embedding Theory Based on a Unique Embedding Potential. *J. Chem. Phys.* **2011**, *134*, 154110.
50. Yu, K.; Libisch, F.; Carter, E. A. Implementation of Density Functional Embedding Theory within the Projector-Augmented-Wave Method and Applications to Semiconductor Defect States. *J. Chem. Phys.* **2015**, *143*, 102806.
51. Yu, K.; Krauter, C. M.; Dieterich, J. M.; Carter, E. A. Density and Potential Functional Embedding: Theory and Practice. In *Fragmentation: Toward Accurate Calculations on*

Complex Molecular Systems; Gordon, M. S., Ed.; John Wiley & Sons: Hoboken, NJ, 2017; pp 81-118.
52. Libisch, F.; Huang, C.; Carter, E. A. Embedded Correlated Wavefunction Schemes: Theory and Applications. *Accounts of chemical research* **2014**, *47*, 2768-2775.
53. Blöchl, P. E. Projector Augmented-Wave Method. *Phys. Rev. B* **1994**, *50*, 17953.
54. Kresse, G.; Furthmüller, J. Efficiency of Ab-Initio Total Energy Calculations for Metals and Semiconductors Using a Plane-Wave Basis Set. *Comput. Mater. Sci.* **1996**, *6*, 15-50.
55. Kresse, G.; Furthmüller, J. Efficient Iterative Schemes for Ab Initio Total-Energy Calculations Using a Plane-Wave Basis Set. *Phys. Rev. B* **1996**, *54*, 11169.
56. Grimme, S.; Antony, J.; Ehrlich, S.; Krieg, H. A Consistent and Accurate Ab Initio Parametrization of Density Functional Dispersion Correction (DFT-D) for the 94 Elements H-Pu. *J. Chem. Phys.* **2010**, *132*, 154104.
57. Grimme, S.; Ehrlich, S.; Goerigk, L. Effect of the Damping Function in Dispersion Corrected Density Functional Theory. *J. Comput. Chem.* **2011**, *32*, 1456-1465.
58. Becke, A. D.; Johnson, E. R. A Density-Functional Model of the Dispersion Interaction. *J. Chem. Phys.* **2005**, *123*, 154101.
59. Makov, G.; Payne, M. C. Periodic Boundary Conditions in Ab Initio Calculations. *Phys. Rev. B* **1995**, *51*, 4014.
60. Monkhorst, H. J.; Pack, J. D. Special Points for Brillouin-Zone Integrations. *Phys. Rev. B* **1976**, *13*, 5188.
61. Methfessel, M.; Paxton, A. T. High-Precision Sampling for Brillouin-Zone Integration in Metals. *Phys. Rev. B* **1989**, *40*, 3616.
62. Henkelman, G.; Uberuaga, B. P.; Jónsson, H. A Climbing Image Nudged Elastic Band Method for Finding Saddle Points and Minimum Energy Paths. *J. Chem. Phys.* **2000**, *113*, 9901.
63. Wu, Q.; Yang, W. A Direct Optimization Method for Calculating Density Functionals and Exchange–Correlation Potentials from Electron Densities. *J. Chem. Phys.* **2003**, *118*, 2498.
64. Werner, H.-J.; Knowles, P. J.; Knizia, G.; Manby, F. R.; Schütz, M. Molpro: A General-Purpose Quantum Chemistry Program Package. *Wiley Interdiscip. Rev. Comput. Mol. Sci.* **2012**, *2*, 242-253.
65. Werner, H.-J.; Knowles, P. J.; Knizia, G.; Manby, F. R.; Schutz, M.; Celani, P.; Gyorffy, W.; Kats, D.; Korona, T.; Lindh, R.; Mitrushenkov, A.; Rauhut, G.; Shamasundar, K. R.; Adler, T. B.; Amos, R. D.; Bernhardsson, A.; Berning, A.; Cooper, D. L.; Deegan, M. J. O.; Dobbyn, A. J.; Eckert, F.; Goll, E.; Hampel, C.; Hesselmann, A.; Hetzer, G.; Hrenar, T.; Jansen, G.; Koppl, C.; Liu, Y.; Lloyd, A. W.; Mata, R. A.; May, A. J.; McNicholas, S. J.; Meyer, W.; Mura, M. E.; Nicklass, A.; O'Neill, D. P.; Palmieri, P.; Peng, D.; Pfluger, K.; Pitzer, R.; Reiher, M.; Shiozaki, T.; Stoll, H.; Stone, A. J.; Tarroni, R.; Thorsteinsson, T.; Wang, M. Molpro, a Package of Ab Initio Programs, version 2015.1. http://www.molpro.net/ (accessed June 1, 2020)
66. Krauter, C. M.; Carter, E. A. EmbeddingIntegralGenerator. https://github.com/EACcodes/EmbeddingIntegralGenerator/ (accessed June 1, 2020)
67. Dunning Jr, T. H. Gaussian Basis Sets for Use in Correlated Molecular Calculations. I. The Atoms Boron through Neon and Hydrogen. *J. Chem. Phys.* **1989**, *90*, 1007.
68. Peterson, K. A.; Puzzarini, C. Systematically Convergent Basis Sets for Transition Metals. II. Pseudopotential-Based Correlation Consistent Basis Sets for the Group 11 (Cu, Ag, Au) and 12 (Zn, Cd, Hg) Elements. *Theor. Chem. Acc.* **2005**, *114*, 283-296.

69. Figgen, D.; Rauhut, G.; Dolg, M.; Stoll, H. Energy-Consistent Pseudopotentials for Group 11 and 12 Atoms: Adjustment to Multi-Configuration Dirac–Hartree–Fock Data. *Chem. Phys.* **2005**, *311*, 227-244.
70. Andersson, K.; Malmqvist, P. A.; Roos, B. O.; Sadlej, A. J.; Wolinski, K. Second-Order Perturbation Theory with a CASSCF Reference Function. *J. Phys. Chem.* **1990**, *94*, 5483-5488.
71. Celani, P.; Werner, H.-J. Multireference Perturbation Theory for Large Restricted and Selected Active Space Reference Wave Functions. *J. Chem. Phys.* **2000**, *112*, 5546.
72. Roos, B. O. The Complete Active Space SCF Method in a Fock-Matrix-Based Super-CI Formulation. *Int. J. Quantum Chem.* **1980**, *18*, 175-189.
73. Siegbahn, P. E. M.; Almlöf, J.; Heiberg, A.; Roos, B. O. The Complete Active Space SCF (CASSCF) Method in a Newton–Raphson Formulation with Application to the HNO Molecule. *J. Chem. Phys.* **1981**, *74*, 2384.
74. Ghigo, G.; Roos, B. O.; Malmqvist, P.-Å. A Modified Definition of the Zeroth-Order Hamiltonian in Multiconfigurational Perturbation Theory (CASPT2). *Chem. Phys. Lett.* **2004**, *396*, 142-149.
75. Roos, B. O.; Andersson, K. Multiconfigurational Perturbation Theory with Level Shift—the Cr_2 Potential Revisited. *Chem. Phys. Lett.* **1995**, *245*, 215-223.
76. Liu, X.; Schlexer, P.; Xiao, J.; Ji, Y.; Wang, L.; Sandberg, R. B.; Tang, M.; Brown, K. S.; Peng, H.; Ringe, S. Ph Effects on the Electrochemical Reduction of $CO(_2)$ Towards C_2 Products on Stepped Copper. *Nat. Commun.* **2019**, *10*, 1-10.
77. Mathew, K.; Sundararaman, R.; Letchworth-Weaver, K.; Arias, T.; Hennig, R. G. Implicit Solvation Model for Density-Functional Study of Nanocrystal Surfaces and Reaction Pathways. *J. Chem. Phys.* **2014**, *140*, 084106.
78. Mathew, K.; Kolluru, V. C.; Mula, S.; Steinmann, S. N.; Hennig, R. G. Implicit Self-Consistent Electrolyte Model in Plane-Wave Density-Functional Theory. *J. Chem. Phys.* **2019**, *151*, 234101.
79. Bader, R. F. A Quantum Theory of Molecular Structure and Its Applications. *Chem. Rev.* **1991**, *91*, 893-928.
80. Tang, W.; Sanville, E.; Henkelman, G. A Grid-Based Bader Analysis Algorithm without Lattice Bias. *J. Phys. Condens. Matter* **2009**, *21*, 084204.
81. Montoya, J. H.; Shi, C.; Chan, K.; Nørskov, J. K. Theoretical Insights into a CO Dimerization Mechanism in CO_2 Electroreduction. *J. Phys. Chem. Lett.* **2015**, *6*, 2032-2037.
82. Huang, Y.; Handoko, A. D.; Hirunsit, P.; Yeo, B. S. Electrochemical Reduction of CO_2 Using Copper Single-Crystal Surfaces: Effects of CO* Coverage on the Selective Formation of Ethylene. *ACS Catal.* **2017**, *7*, 1749-1756.

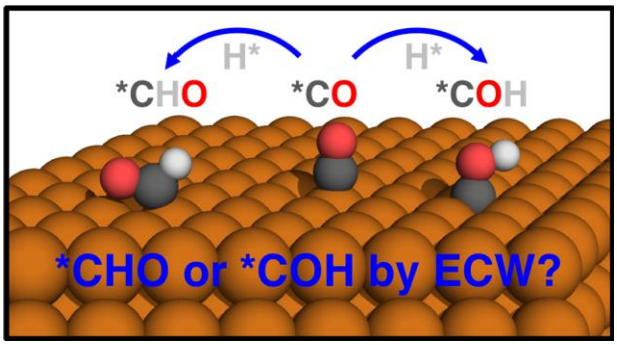

For Table of Contents Only